Available online at www.sciencedirect.com
SCIENCE DIRECT®
Journal of Power Sources 140 (2005) 235–242
JOURNAL OF POWER SOURCES
www.elsevier.com/locate/jpowsour

Computational analysis of species transport and electrochemical characteristics of a MOLB-type SOFC

J.J. Hwang[a,*], C.K. Chen[b], D.Y. Lai[b]

[a] *Research Center for Advanced Science and Technology, Mingdao University, Changhua 523, Taiwan*
[b] *Department of Mechanical Engineering, National Cheng Kung University, Tainan 701, Taiwan*

Received 13 July 2004; received in revised form 16 August 2004; accepted 16 August 2004
Available online 18 October 2004

Abstract

A multi-physics model coupling electrochemical kinetics with fluid dynamics has been developed to simulate the transport phenomena in mono-block-layer built (MOLB) solid oxide fuel cells (SOFC). A typical MOLB module is composed of trapezoidal flow channels, corrugated positive electrode-electrolyte-negative electrode (PEN) plates, and planar inter-connecters. The control volume-based finite difference method is employed for calculation, which is based on the conservation of mass, momentum, energy, species, and electric charge. In the porous electrodes, the flow momentum is governed by a Darcy model with constant porosity and permeability. The diffusion of reactants follows the Bruggman model. The chemistry within the plates is described via surface reactions with a fixed surface-to-volume ratio, tortuosity and average pore size. Species transports as well as the local variations of electrochemical characteristics, such as overpotential and current density distributions in the electrodes of an MOLB SOFC, are discussed in detail.
© 2004 Elsevier B.V. All rights reserved.

Keywords: SOFC; Model; Transport phenomena

1. Introduction

Fuel cells are drawing keen attention for their high efficiency and eco-friendly characteristics. Among fuel cells, solid oxide fuel cells (SOFCs) are less sensitive to fuel composition compared to other fuel cell systems. Besides the reformed gas from the external reformer, the anode feed of SOFC can employ natural gas, LPG, methanol, or coal gas through internal reforming on the anode side.

A typical SOFC operates at a temperature between 700 and 1000 °C. Such a high temperature accelerates the electrochemical reaction; therefore, SOFCs do not require precious metal catalysts to enhance the reaction. In addition, SOFCs can attain an electric efficiency as high as 65%, surpassing the 50% achieved by LNG compound-power generation because of its ability to be used in combination with gas turbines using high-temperature gas exhaust.

SOFCs, like any other electrochemical device, consist of two electrodes (anode and cathode), and an electrolyte, which allows transfer of oxygen ions. These three layers are laminated into a single positive electrode/electrolyte/negative electrode (PEN) plate. The PEN plates are then connected in a series stack via inter-connect plates. As shown in Fig. 1, the PEN plate can be molded unevenly in a trapezoidal or dimple shape, which is known as mono-block layer built (MOLB) SOFC. Such a design has benefits in enhancing its mechanical strength and increasing its power density. The corrugated-shaped PEN plate not only ensures that the effective active area is higher than the projected area, but also provides the film with the combined function of fuel and airflow paths, making the cell compact.

For optimal design and operation of MOLB-type SOFCs, a comprehensive understanding of transport and electrochemical characteristics is highly essential. However, previous

* Corresponding author. Tel.: +886 4887 660x8302.
E-mail address: azaijj@mdu.edu.tw (J.J. Hwang).

0378-7753/$ – see front matter © 2004 Elsevier B.V. All rights reserved.
doi:10.1016/j.jpowsour.2004.08.028

Nomenclature

a'	stoichiometric coefficient of the products
a''	stoichiometric coefficient of the reactants
D	diffusivity ($m^2\ s^{-1}$)
F	Faraday's constant (96487 C mol^{-1})
$\boldsymbol{i}$	current density ($A\ m^{-2}$)
$\boldsymbol{j}$	transfer current density ($A\ m^{-3}$)
$\boldsymbol{J}$	diffusive flux ($kg\ s^{-1}\ m^{-2}$)
k	thermal conductivity ($W\ K^{-1}\ m^{-1}$)
M	molecular weight ($kg\ mol^{-1}$)
p	pressure (Pa)
R	universal gas constant ($W\ mol^{-1}\ K^{-1}$)
T	temperature (K)
$\boldsymbol{U}$	velocity vectors ($m\ s^{-1}$)
X, Y, Z	coordinate system, Fig. 1 (m)
X_i	fraction of molar concentration of species i
Y_i	mass fraction of species of i

Greek symbols

Φ	solid-phase potential (V)
α	symmetric factor
σ	electric conductivity ($\Omega^{-1}\ m^{-1}$)
ε	porosity
κ	permeability (m^2)
ρ	density ($kg\ m^{-3}$)
η (or Over_P)	overpotential, $\Phi_{\mathbf{C}} - \Phi_{\mathbf{E}}$ (V)
μ	viscosity ($m\ s^{-2}$)

Subscripts

A	anode
C	catalyst or cathode
eff	effective
E	electrolyte
F	fluid
i	species
ref	reference
S	solid
T	transfer current

studies are mostly for either planar or tubular SOFCs [1–7], and so far have not yet considered the geometry of MOLB-type SOFCs. The present study aims to develop a CFD-based model to resolve the complex interaction between fluid dynamics and electrochemical kinetics in a MOLB-type SOFC. In contrast to the results obtained from models that specify uniform surface overpotential [4,8], the present model implements the voltage-to-current algorithm that allows for a more realistic spatial variation of electrochemical kinetics. This results in an improved prediction of local overpotential and current density distributions.

2. Model development

2.1. Basics of MOLB-type SOFC

A typical single-cell module of the MOLB-type SOFC consists of a PEN plate and an inter-connect (Fig. 1). The fuel and air run in a counter current direction in the trapezoidal channels that are separated by a corrugate PEN plate. The oxidant reduction reaction occurring in the cathode is expressed as follows.

$$O_2 + 4e^- \rightarrow 2O^{2-} \tag{1}$$

The oxygen ion is then transported through the electrolyte and then into the active anode. The electrochemical reactions of H_2 and CO on anode catalysts are:

$$H_2 + O^{2-} \rightarrow H_2O + 2e^- \tag{2}$$

$$CO + O^{2-} \rightarrow CO_2 + 2e^- \tag{3}$$

The co-oxidations of Eqs. (2) and (3) are limited to a single-step reaction in the present model, i.e.,

$$H_2 + CO + 2O^{2-} \rightarrow H_2O + CO_2 + 4e^- \tag{4}$$

2.2. Model equations

The continuity, momentum, and species conservations are modeled as:

$$\nabla \cdot (\varepsilon\rho\boldsymbol{U}) = \mathbf{0} \tag{5}$$

$$\nabla \cdot (\varepsilon\rho\boldsymbol{U}\boldsymbol{U}) = -\varepsilon\nabla p + \nabla \cdot (\varepsilon\mu_{\text{eff}}\nabla\boldsymbol{U}) + \frac{\varepsilon^2\mu\boldsymbol{U}}{\kappa} \tag{6}$$

$$\nabla \cdot (\varepsilon\rho\boldsymbol{U}Y_i) = \nabla \cdot \boldsymbol{J}_i + (a_i'' - a_i')\frac{\boldsymbol{j}_{\text{T}}}{F} \tag{7}$$

The isotropic linear resistance model of Darcy's law with constant porosity (ε) and permeability (κ) is used to govern the momentum equation. The diffusive mass flux $\boldsymbol{J}_i$ is described by the Stefan–Maxwell equation [9]. The effective diffusivities in the multi-component mixture system follow the Bruggman model [10]. a''_i and a'_i are the stoichiometric coefficients of the products and reactants, respectively. The electrode electrochemistry and the species transport kinetics are connected by the Butler–Volmer equation [11] on the surfaces of the active layers, i.e.,

$$\boldsymbol{j}_{\text{T,A}} = \boldsymbol{j}_{0,\text{A}} \left\{ \left(\frac{X_{\text{H}_2}}{X_{\text{H}_2,\text{ref}}} \right)^{1/4} \left(\frac{X_{\text{CO}}}{X_{\text{CO,ref}}} \right)^{1/4} \exp\left[\frac{\alpha_{\text{A}} F}{RT}\eta \right] - \left(\frac{X_{\text{H}_2\text{O}}}{X_{\text{H}_2\text{O,ref}}} \right)^{-1/4} \left(\frac{X_{\text{CO}_2}}{X_{\text{CO}_2,\text{ref}}} \right)^{-1/4} \times \exp\left[\frac{-(1-\alpha_{\text{A}})F}{RT}\eta \right] \right\} \tag{8}$$

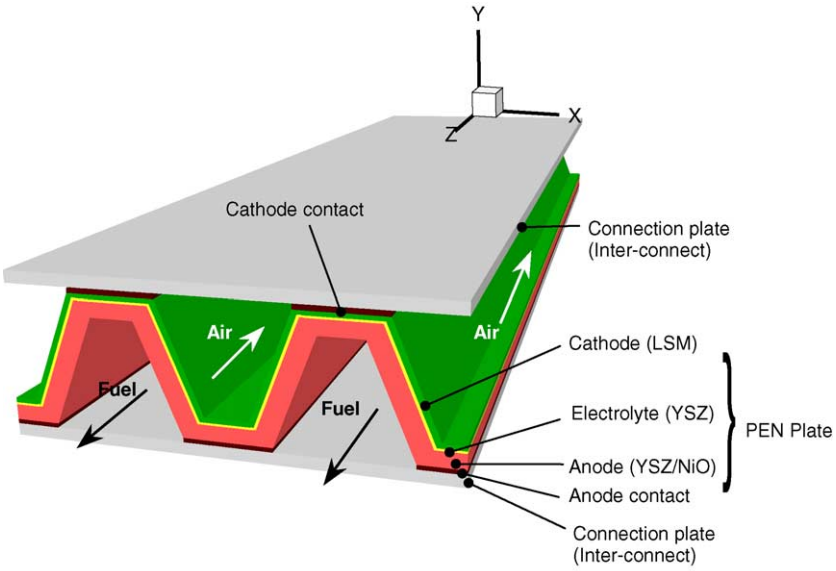

Fig. 1. Schematic diagram of a single-cell module of the MOLB-type SOFC.

$$\boldsymbol{j}_{\mathrm{T,C}} = \boldsymbol{j}_{0,\mathrm{C}}\left(\frac{X_{\mathrm{O_2}}}{X_{\mathrm{O_2,ref}}}\right)^{1/4} \exp\left(\frac{-\alpha_{\mathrm{C}} F}{RT}\eta\right) \tag{9}$$

where η is the electrode overpotential, $\boldsymbol{j}_{0,\mathrm{A}}$ and $\boldsymbol{j}_{0,\mathrm{C}}$ the anodic and cathodic exchange current densities, respectively, and α_{A} and α_{C} are the anodic and cathodic Tafel constants, respectively.

In the active layer, a potential difference exists between the catalyst ($\Phi_{\mathbf{C}}$) and electrolyte ($\Phi_{\mathbf{E}}$) to drive the transfer current ($\boldsymbol{j}_{\mathrm{T,A}}$ or $\boldsymbol{j}_{\mathrm{T,C}}$), keeping the electrochemical reaction continuously. As shown in Fig. 2, the current passes through the electrode can be decomposed two parts, i.e.,

$$\boldsymbol{i} = \boldsymbol{i}_{\mathrm{C}} + \boldsymbol{i}_{\mathrm{E}} \tag{10}$$

These two current components interact through the electrochemical reaction. The electrons are either transferred to the catalyst from the electrolyte or vice versa during the reaction. Application of Ohm's law to Eq. (10) yields the current conservation:

$$\nabla \cdot (\boldsymbol{i}_{\mathrm{C}}) = \nabla(-\sigma_{\mathrm{eff,C}} \nabla \Phi_{\mathrm{C}}) = -\boldsymbol{j}_{\mathrm{T}} \tag{11}$$

$$\nabla \cdot (\boldsymbol{i}_{\mathrm{E}}) = \nabla(-\sigma_{\mathrm{eff,E}} \nabla \Phi_{\mathrm{E}}) = \boldsymbol{j}_{\mathrm{T}} \tag{12}$$

where $\sigma_{\mathrm{eff,C}}$ and $\sigma_{\mathrm{eff,E}}$ are the effective electric conductivities of the catalyst and electrolyte in the electrode, respectively. Physical properties and parameters used in the present model are summarized in Tables 1 and 2.

3. Numerical implementation

As shown in Fig. 3, a typical MOLB unit is symmetric about the mid-planes of the air and fuel channels. Therefore, the present computational domain covers the region between these two planes for memory and time saving. The governing equations were numerically solved by the control volume-based finite difference method [12]. The discretization procedure ensures conservation of mass, momentum, and concentration over each control volume. The coupling of the pressure and velocity fields was treated via the SIMPLER pressure correction algorithm [13,14]. The upwind difference scheme was used to treat the convection and diffusion

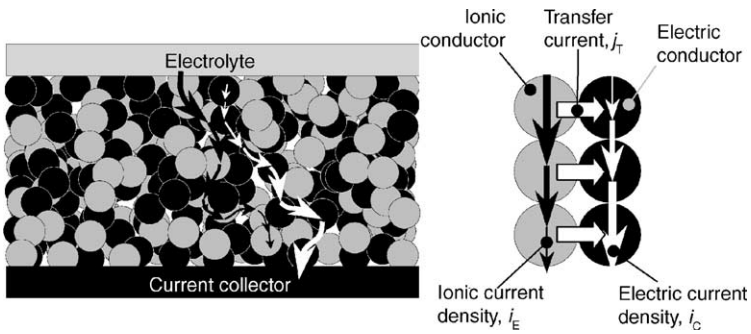

Fig. 2. Scheme of the transfer current in the SOFC electrode.

Table 1
Porous-chemistry properties of the electrodes

Description	Unit	Value
Anode exchange current, $\boldsymbol{J}_{0,A}$	$A\,m^{-3}$	1.0×10^{9}
Cathode exchange current, $\boldsymbol{J}_{0,C}$	$A\,m^{-3}$	5.0×10^{7}
Anode transfer coefficient, α_A	–	1.0
Cathode transfer coefficient, α_C	–	1.0
Anode stoichiometric coefficient	–	3.0
Cathode stoichiometric coefficient	–	5.0
Anode inlet mass flow rate	$kg\,s^{-1}$	1.19×10^{-6}
Cathode inlet pressure	$kg\,s^{-1}$	4.74×10^{-8}
Anode inlet pressure	kPa	1.013×10^{5}
Cathode inlet pressure	kPa	1.013×10^{5}
Stack temperature	K	973
Species molar concentration at anode inlet		
Hydrogen, X_{H_2}	%	45.57
Carbon monoxide, X_{CO}	%	6.97
Carbon dioxide, X_{CO_2}	%	6.55
Water, X_{H_2O}	%	36.84
Methane, X_{CH_4}	%	4.07
Total	%	100
Species molar concentration at cathode inlet		
Oxygen, X_{O_2}	%	21.11
Nitrogen, X_{N_2}	%	78.99
Total	%	100

terms. Solutions were considered to be converged after the ratio of residual source (including mass, momentum, species, and current) to the maximum flux across a control surface is less than 1.0×10^{-3}. The computations were performed on $18 \times 40 \times 50$ (X by Y by Z) structured, orthogonal meshes in the present work (Fig. 3). A typical simulation required about 500 min of central processing unit time on a Pentium IV 2.0 GHz PC.

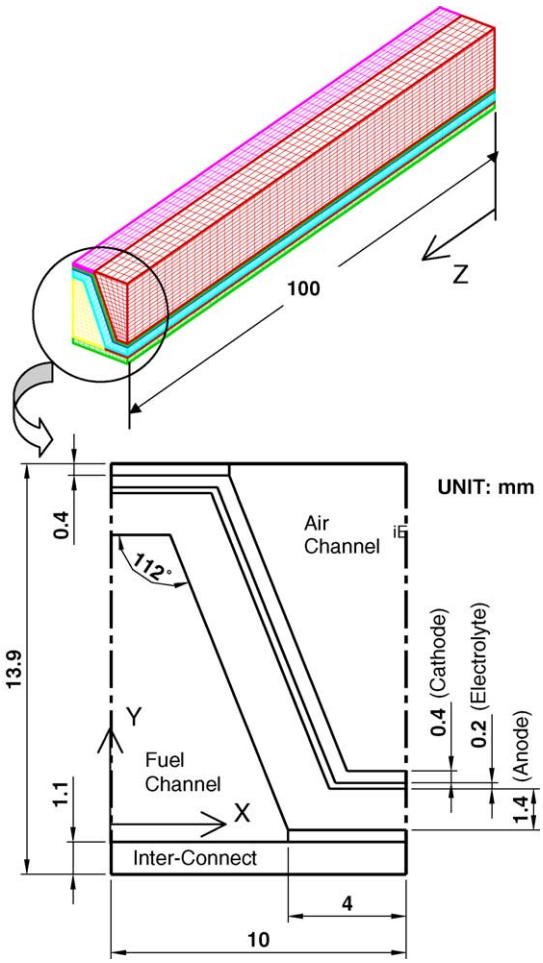

Fig. 3. Dimensions, coordinate system, and grid distribution of the computational domain.

4. Results and discussion

Conditions for the present calculation are to achieve average cell temperature of 973 °C. Air and fuel delivered to the cathode and anode are $2.975 \times 10^{-5}\,kg\,s^{-1}$ and $1.185 \times 10^{-6}\,kg\,s^{-1}$, respectively. These correspond to the stoichiometric flow ratios 5.0 and 3.0 at the current density of $1.0\,A\,cm^{-2}$, respectively. The molar composition of the fuel is 45.57%/6.97%/6.55%/36.84%/4.07% for H_2/CO/CO_2/H_2O/CH_4. The voltage drop across the module is set at 0.4 V in the present computation.

Fig. 4 displays the distribution of oxygen mass fraction (Y_{O_2}) on the interface between the air channel and the cathode. It is observed that the high oxygen mass fraction from the entrance of the channel inlet decreases along the axial distance ($-Z$) due to the oxygen reduction reaction. The oxygen mass fraction has a local minimum at the channel corner formed by the inclined and bottom planes. The forced convection in the local minimum is weak due to the corner effect. Another corner formed by the inclined plane and the upper plane does not sense the local minimum. It is clearly seen

Table 2
Physical properties in the porous electrodes

Description	Anode	Cathode	Electrolyte	Electrode contact	Inter-connector
Thickness (mm)	1.4	0.4	0.2	0.4	0.5
Porosity ε	0.4	0.5	1.0×10^{-5}	0.3	1.0×10^{-5}
Permeability, κ (m^2)	1.0×10^{-12}	1.0×10^{-12}	1.0×10^{-18}	1.0×10^{-12}	1.0×10^{-18}
Tortuosity	1.5	1.5	6	1.5	6
S/V (m^{-1})	1000	1000	–	–	–
Pore size (m)	1.0×10^{-6}	1.0×10^{-6}	1.0×10^{-6}	1.0×10^{-6}	1.0×10^{-6}
Effective thermal conductivity, k_{eff} ($W\,m^{-1}$)	6.23	9.6	2.7	60.7	9.6
Effective electric conductivity, σ_{eff} ($\Omega^{-1}\,m^{-1}$)	1.0×10^{5}	7.7×10^{3}	1.0×10^{-20}	1.56×10^{7}	1.35×10^{6}

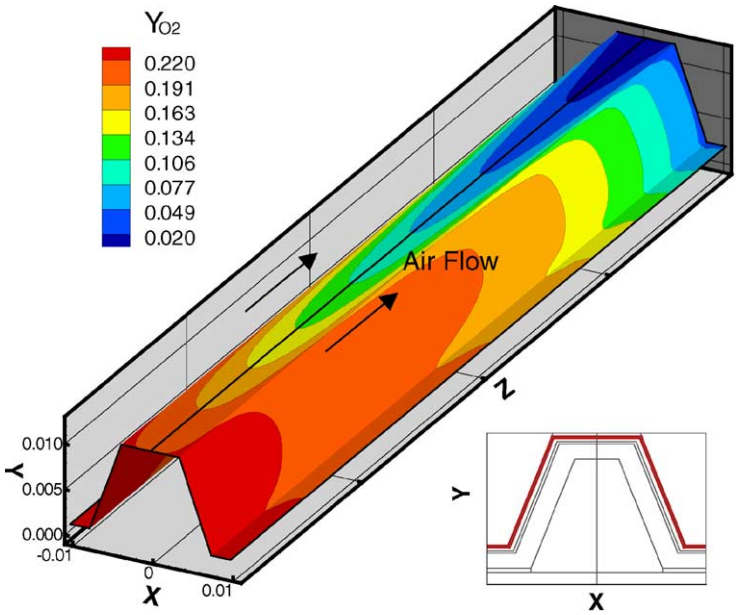

Fig. 4. Oxygen concentration distributions at the interface of the channel and the cathode.

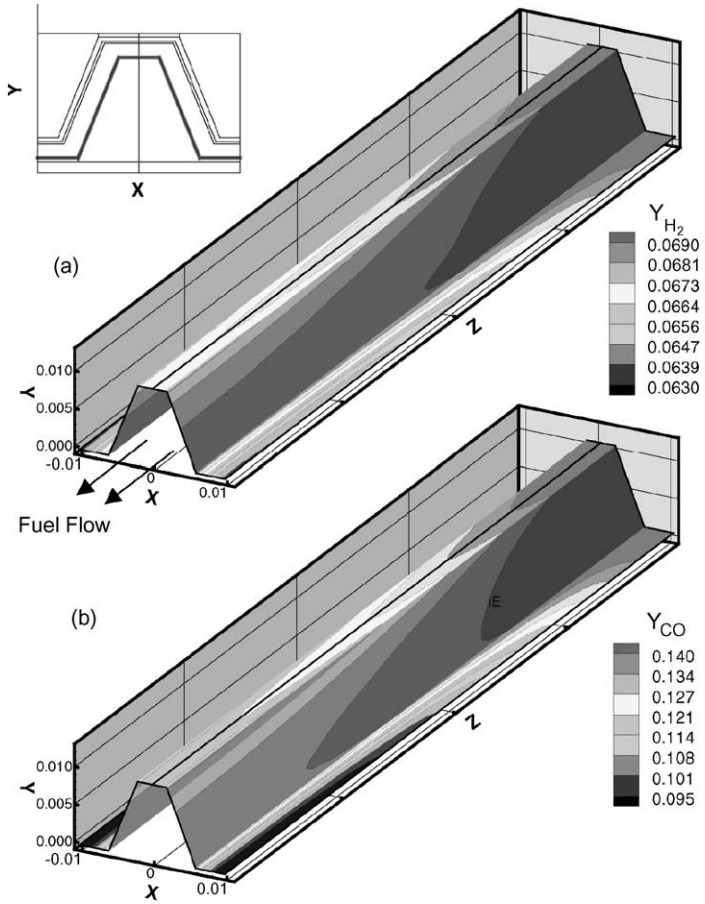

Fig. 5. Reactant concentration distributions on the interface between channel and the anode (a) hydrogen and (b) carbon monoxide.

that the iso-line of O_2 mass fraction extends from the mid-inclined-plane to the plateau center, which is in touch with the cathode contact through the upper channel corner. Since the air-flow is retarded by the porous matrix of the cathode contact, the fresh air cannot move into the upper plateau easily. This results in a lack of reactants for electrochemical reaction. In this circumstance, a significant overpotential will arise to operate normally in this region, which will be shown later. It can be concluded that the oxygen transport is dominated by convection on both surfaces of the inclined and bottom planes. In contrast, the oxygen transport along the plateau is mainly achieved by diffusion.

Fig. 5 shows the distribution of mass fraction of hydrogen (Y_{H_2}) and carbon monoxide (Y_{CO}) on the surfaces of the channel-anode interface. It can be seen that both Y_{H_2} and Y_{CO} gradually decrease due to the chemical reaction along the channel distance. The local minima of Y_{H_2} and Y_{CO} also occur at the corner formed by the inclined and ceiling planes and at the mid-plane of the bottom plane where H_2 and CO are transported mainly through diffusion.

Fig. 6a and b shows the overpotential distributions on the mid-planes of the cathode and anode, respectively. In the anode, the positive overpotential directs the transfer current from the catalyst to the electrolyte, and vice versa in the cathode. In general, the cathode needs higher energy in order to activate the reactants. The absolute value of the overpotential in the cathode is significantly higher than that in the anode. It can be seen that the overpotential is higher near the exit of the oxidant flow where it coincides with the regions of lower oxygen concentration on the cathode plane. Depletion of reactants results in an increase of overpotential along the channel. At a fixed axial distance, the maximum overpotential occurs at the plateau center where the oxygen is almost used up (Fig. 4).

Fig. 7a and b compares the current density distribution on the mid-planes of the cathode and anode. These plots cover only the mid-quarter channel results. The arrows attached on the plane surfaces are the projections of the current density vectors at the corresponding position. These arrows indicate not only the direction but also the relative magnitude of the

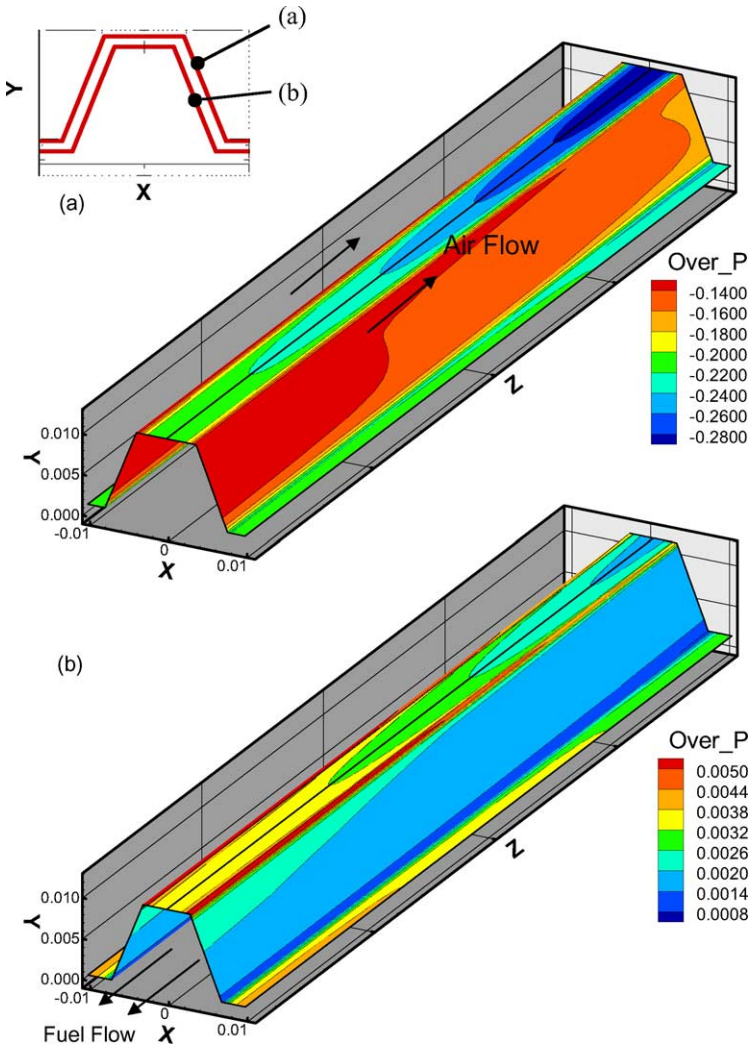

Fig. 6. Overpotential distributions on the mid-planes of the electrodes (a) cathode and (b) anode.

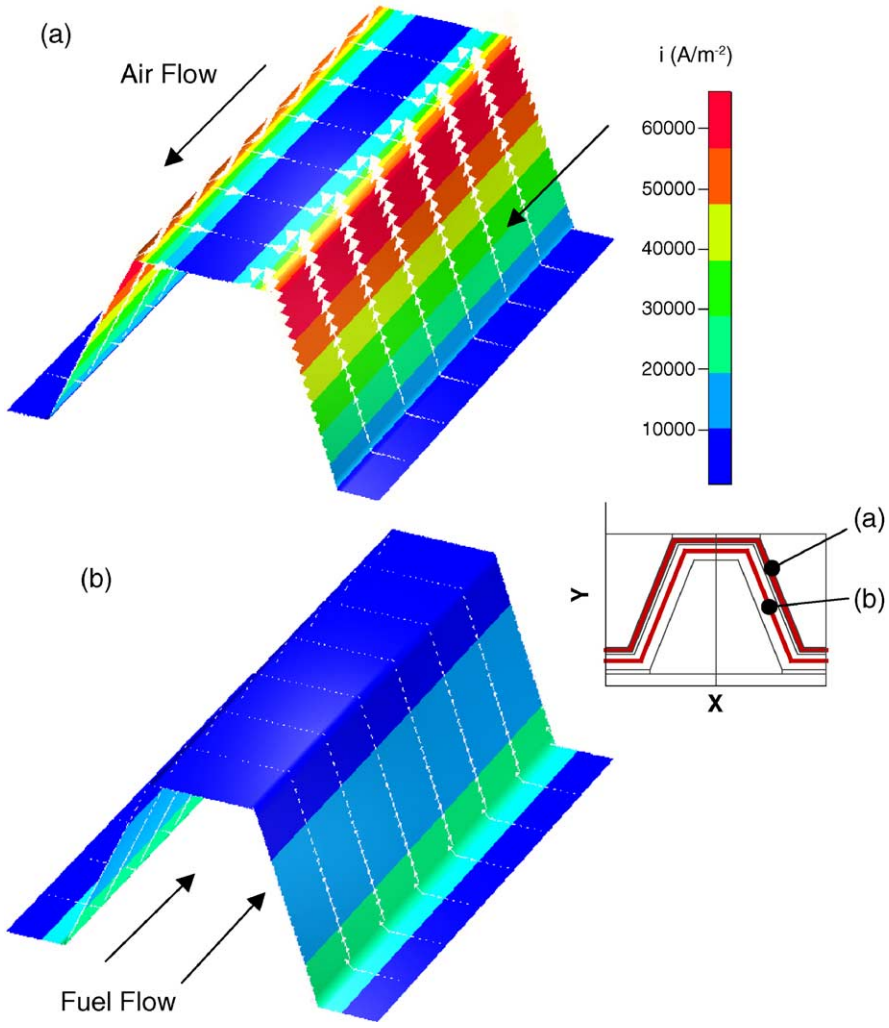

Fig. 7. Distributions of current density on the mid-plane surfaces of electrodes (a) cathode and (b) anode.

currents. Attention is placed on the inclined planes first. On the inclined plane of the anode, the current density gradually decreases along the current direction, since the current transfers from the high-potential catalyst (electronic conductor) to the low-potential electrolyte (ionic conductor). Conversely, the current density gradually increases along the current direction on the cathode plane because of the current accumulation by transferring the current from the ionic conductor to the electronic conductor. In the present model, the anode-supported PEN plane has a thick anode, thus, resulting in a current passage with a larger cross-sectional area. This reduces the current density. The top and the bottom planes have a relatively large area for the passing through current, which directs upward for both electrodes. As a result, the current density is rather small in these regions.

5. Conclusions and future work

This paper has presented a computational simulation of the fluid dynamics and electrochemical kinetics in a MOLB-type SOFC. Significant results about the local transport characteristics inside the MOLB-type SOFC, such as the reactant gas concentration distribution, the overpotential distribution, and the current density distribution have been presented. The unique features of this model are the implementation of the voltage-to-current algorithm and the coupling of the potential field with the reactant species concentration field, which allows for a more realistic spatial variation of the electrochemical kinetics. The spatial variation of the cathodic and anodic surface overpotential is computed locally, thus, resulting in an improved prediction of the local current density distribution. These local current density distribution patterns are radically different from those obtained from models that do not account for the non-uniformity of the surface overpotential.

Acknowledgments

This work was sponsored by the National Science Council of Taiwan under contract no. NSC 92-2212-E-451-002.

References

[1] W. Lehnert, J. Meusinger, F. Thom, J. Power Sources 87 (2000) 57–63.
[2] Z. Lin, J.W. Stevenson, M.A. Khaleel, J. Power Sources 117 (2003) 92–97.
[3] K.P. Recknagle, R.E. Williford, L.A. Cgick, D.R. Rector, M.A. Khaleel, J. Power Sources 113 (2003) 109–114.
[4] H. Yakabe, T. Ogiwara, M. Hishinuma, I. Yasuda, J. Power Sources 86 (2001) 144–154.
[5] H. Yakabe, M. Hishinuma, M. Uratani, Y. Matsuzaki, I. Yasuda, J. Power Sources 86 (2000) 423–431.
[6] S. Campanari, J. Power Sources 92 (2001) 26–34.
[7] M. Lockett, M.J.H. Simmons, K. Kendall, J. Power Sources 131 (2004) 243–246.
[8] J.J. Hwang, C.K. Chen, R.F. Savinell, C.C. Liu, J. Wainright, J. Applied Electrochem. 34 (2004) 217–224.
[9] S.C. Singhal, K. Kendall, High-Temperature Solid Oxide Fuel Cells: Fundamentals, Design and Applications, Elsevier Science Pub Co., 2004.
[10] J. Bear, J.M. Buchlin, Modeling and Application of Transport Phenomena in Porous Media, Kluwer Academic Publishers, Boston, MA, 1991.
[11] P. Costamagna, K. Honegger, J. Electrochem. Soc. 145 (1998) 3995.
[12] S.V. Patankar, Numerical Heat Transfer and Fluid Flow, Hemisphere, New York, 1980.
[13] J.P. Van Doormaal, G.D. Raithby, Numerical Heat Mass Transfer, Part A 7 (1992) 147–163.
[14] J.J. Hwang, D.Y. Lai, Int. J. Heat Mass Transfer 41 (1998) 979–991.